Materials & Design 252 (2025) 113817

Contents lists available at ScienceDirect

Materials & Design

journal homepage: www.elsevier.com/locate/matdes

Enhancing the efficiency of luminescent solar concentrators via soft colloidal lithography negative templating

J.G. Guerrero-Felix [a,b,1], S.F.H. Correia [c,1], M. Alexandre [d], C.D. Gonzalez-Gomez [a,e], V. Sencadas [f], L. Fu [g], E. Ruiz-Reina [e], P.S. André [i], C.L. Moraila-Martinez [b,h], M.J. Mendes [d], R.A.S. Ferreira [g,*], M.A. Fernandez-Rodriguez [a,*]

[a] Department of Applied Physics, Faculty of Sciences, University of Granada, Campus de Fuentenueva s/n, Granada, 18071, Spain
[b] Faculty of Biology, Autonomous University of Sinaloa, Campus Universitario, Culiacan, 80010, Sinaloa, Mexico
[c] Instituto de Telecomunicações and University of Aveiro, 3810-193 Aveiro, Portugal
[d] i3N/CENIMAT, Department of Materials Science, NOVA School of Science and Technology and CEMOP/UNINOVA, Campus de Caparica, 2829-516, Caparica, Portugal
[e] Department of Applied Physics II, University of Malaga, Campus de Teatinos, Malaga, 29071, Spain
[f] Department of Materials and Ceramic Engineering and CICECO - Aveiro Institute of Materials, University of Aveiro, 3810-193, Aveiro, Portugal
[g] Department of Physics and CICECO - Aveiro Institute of Materials, University of Aveiro, 3810-193, Aveiro, Portugal
[h] Department of Electronics and Computer Technology, Faculty of Sciences, University of Granada, Campus de Fuentenueva s/n, Granada, 18071, Spain
[i] Department of Electrical and Computer Engineering, Instituto de Telecomunicações, University of Lisbon, 1049-001, Lisbon, Portugal

ARTICLE INFO

Keywords:
Building-Integrated Photovoltaics
Luminescent Solar Concentrators
Soft Colloidal Lithography

ABSTRACT

Building-integrated photovoltaics (BIPV) offers a sustainable pathway by seamlessly incorporating PV cells into architectural elements like façades and windows. In this study, we investigate the potential of luminescent down-shifting solar concentrators in combination with a nanophotonic light-trapping scheme to improve the optical-guiding capabilities and thereby enhance the energy conversion efficiency. We propose a novel cost-effective method to fabricate the photonic structures via soft colloidal lithography negative templating of thin films of TiO_2 nanoparticles, successfully scaling the production to 11x11 cm^2 glass windows. Through simulations and optical-electrical characterization, we demonstrate substantial improvements in energy harvesting for different angles of solar irradiation. We found increases in power output ranging from 57% for angles of incidence below 45° to above 100% for 60° thanks to the nanostructured TiO_2 nanoparticles coatings added to a bottom down-shifting layer. This shows that such integrated approach can enhance both the efficiency and aesthetic appeal of solar solutions in urban environments, advancing the design of energy-efficient, sustainable buildings. Our methodology ensures consistent solar energy capture all year-round, for the relevant range of sunlight incidence angles, while preserving the transparency and multifunctionality of building elements.

1. Introduction

We rely worldwide on photovoltaic cells (PV) as highly effective devices to provide renewable energy in our fight against climate change. In our cities, we need to consider the PV cells as construction elements, e.g. in the roofs, façades and windows of our buildings. In building-applied photovoltaics (BAPV), the PV cells are mounted as external components on the building. In contrast, in building-integrated photovoltaics (BIPV), the PV cells are built directly into the building structure. While BAPV is more widely developed and commonly used, particularly on rooftops, BIPV offers a promising approach to minimize the visual and structural impact of PV cells in everyday life [1–8]. A crucial factor for the successful integration of BIPV, particularly in terms of public acceptance, is their apparent invisibility. This means that the PV devices should blend seamlessly into the building's design without compromising its aesthetics or diminishing the quality of life for occupants by obstructing natural sunlight [4]. Moreover, PV cells designed for integration into vertical façades and windows must be engineered to handle indirect and glazing angle solar irradiation [9–11].

* Corresponding authors.
E-mail addresses: rferreira@ua.pt (R.A.S. Ferreira), mafernandez@ugr.es (M.A. Fernandez-Rodriguez).
[1] These authors contributed equally to this work.

https://doi.org/10.1016/j.matdes.2025.113817
Received 8 January 2025; Received in revised form 19 February 2025; Accepted 5 March 2025

Available online 10 March 2025

Luminescent solar concentrators (LSCs) are driving a green architecture revolution by enabling PV cells to be integrated along the edges of transparent windows. This transforms windows into distributed power generators, without compromising the building aesthetics [12–16]. LSCs are semi-transparent materials coated or doped with chromophores, thus being optically active with capability to absorb and re-emit sunlight. When applied as windows, LSCs can guide the light towards the window edges where conventional thin PV cells are positioned. By combining fluorescence with total internal reflection (TIR), LSCs effectively redirect light, making them resilient to shading caused by trees, streetlights, or chimneys, which typically degrade the performance of conventional PV systems. [1,17–20]. Furthermore, LSCs integrate spectral converters to enhance the performance of PV devices. One particularly effective converter is the down-shifting layer (DSL), which transforms ultraviolet light (UV), typically absorbed by the glass or plastic in the window, into visible light. This visible light is then directed towards the PV cells at the edges of the window, improving the overall energy harvesting [21,3]. A key advantage of LSCs, and DSLs specifically, is their ability to perform consistently under both direct and diffuse sunlight. Additionally, their design is highly versatile, as they can be applied as a coating that conforms to any surface, making them suitable for a wide range of architectural applications [4]. Despite the efficiency gains from harvesting the diffuse light, there is still a substantial amount of direct solar irradiance that reaches vertical façades. In fact, during certain times of the year, this direct irradiance can even surpass the horizontal irradiance received on roofs [22].

The performance of DSLs is highly dependent on the optically active layer but also limited by the geometrical and optical aspects of the lightguide coating. Thus, the light trapping efficiency is one of the key parameters to take into account [3,23]. In polymer planar lightguides with refractive index of 1.5, chosen to index-match the glass in windows, a theoretical maximum of 75% of the down-shifted light is trapped in the lightguide via TIR. The remaining 25% of down-shifted light is lost through the escape cone [24,25]. One way to increase the trapping efficiency in DSLs is by nanostructuring the lightguide surface [26–29]. Such synergistic integration has been explored for the emergent perovskite-based PV technology, namely by optimizing photonic-structured front contacts overcoated with encapsulanting films embedded with DSL nanoparticles [13,30]. Additionally, the nanostructured DSLs can reduce reflection losses as well as provide passive cooling [31–35].

Recently, nanostructured PV cells fabricated using organic materials have captured attention due to the abundance, low-cost, and non-toxicity of these nanomaterials. Their primary issue is the degradation over time under the sunlight [36,37]. A possible solution is switching to inorganic materials for the nanostructured coatings, such as the ones fabricated via conventional lithography in clean rooms. For example, vertically aligned nanowires can increase the surface area of solar devices and improve the light trapping, but their fabrication relies on complex and expensive equipments, making it less practical for large-scale production [38]. As an example, the electron-beam lithography technique is highly precise, but the process is slow and confined to millimeter-scale areas, limiting its use mainly to research and high-value applications [39]. Furthermore, nanoimprint uses a stamp to imprint nanostructures onto the substrates, which is faster and cost-effective, but the fabrication of the stamps suffers from the same issues described so far, plus concerns on the stamp durability and alignment accuracy that can impact the quality of the nanostructures [40,41]. Thus, although inorganic nanostructuring can improve the efficiency in BIPV, scalability and costs are common issues when considering conventional lithography techniques.

Colloidal lithography offers an attractive alternative, being nowadays regarded as one of the soft-patterning methods with highest potential for nano/micro-structuring in PV industry [41]. Colloidal lithography methods rely on the spontaneous self-assembly of nano or microparticle monolayers at liquid interfaces and their transfer to substrates to create nano/micro-structured surfaces that can have strong light trapping capabilities [42–44]. It is cost-effective and inherently scalable due to the spontaneous self-assembly of nanoparticle monolayers at interfaces, without the need of clean room conditions nor expensive equipment. The main disadvantage is achieving uniformity and controlling the size distribution of the nanostructures [45,46]. In order to tackle these issues, we propose to use a soft colloidal lithography (SCL) approach. In SCL we use microgels as building blocks, which are soft nanoparticles made of crosslinked hydrogels. The main advantage is that the self-assembly of microgels at liquid interfaces creates highly ordered arrays that are easily transferred to solid substrates thanks to the self-healing properties of the elastic monolayers. In previous works, some of us showed that the SCL can be used to obtain large-area complex nanostructured patterns without the need for expensive equipment nor clean room conditions. A great variety of self-assembled nanostructures can be achieved by adjusting the size and composition of the microgels, the compression of the monolayer, and with additional strategies such as sequential depositions [47–49].

In this study, an unprecedented combination of DSL and photonic nanostructuring is assessed for application in cost-effective LSC technology. We develop a new SCL technique to fabricate inorganic nanostructured coatings composed of TiO_2 nanoparticles, via SCL negative templating. We use these nanostructured inorganic coatings to enhance the light trapping of DSL-based BIPV in windows. Given the prime importance of the fabrication of real-world-sized devices, this novel technique was scaled-up from glass slides on a Langmuir-Blodgett trough to 11×11 cm^2 windows. We then explore the role of having a nanostructured TiO_2 coating ($nTiO_2$), assisted by SCL negative templating, compared to a homogeneous coating ($hTiO_2$), plus having an additional DSL layer on top (tDSL) or at the bottom (bDSL) of the glass window, with conventional PV cells installed on the sides of the window. We find a significant synergistic effect, where the enhanced light trapping and scattering properties of the $nTiO_2$ coatings enhance the efficiency of the down-shifting spectral conversion of the DSLs.

2. Materials and methods

2.1. Materials

For the DSLs, we used TFNB (Aldrich) and BBA (Aldrich), Phen (Alfa-Aesar), sodium hydroxide (NaOH), hydrochloride acid (HCl), and ethanol (EtOH). We obtained an Europium chloride ($EuCl_3$, 0.2 M) aqueous solution by dissolving europium oxide (Eu_2O_3, Yuelong New Material Co., Ltd., Shanghai, China) in HCl (37%, Aldrich). We removed the remaining acid by successive evaporation and dissolved the resulting solid in Milli-Q water. The SEBS material (Calprene H6180X, with 85/15 ethylene butylene/styrene ratio) was supplied by the Dynasol Group.

The inorganic nanoparticles for the nanostructured thin layers that we used in this study are titanium(IV) oxide (TiO_2) nanoparticles dispersed in water, consisting of a mixture of rutile and anatase (40%, Sigma Aldrich). We synthesized the microgels for the soft colloidal lithography negative templating by precipitation polymerization. The synthesis involved N-vinylcaprolactam (4.52 g, VCL, 98%, Sigma Aldrich) as monomer, N-methylenebisacrylamide (0.0816 g, BIS, 99.5%, Sigma Aldrich) as crosslinker to obtain a crosslinking density of 1.6% mol, and 2,2'-azobis (2-amidinopropane) dihydrochloride (0.0816 g, V50, 98%, Acros) as initiator, all dissolved in 200 mL of Milli-Q water. After adding the initiator the reaction was kept for 7 h under N_2 flow at 60°C. At the end, the microgels were centrifuged 3 times at 39400 rcf replacing the supernatant by Milli-Q water. We used isopropyl alcohol (99.8%, Sigma Aldrich) as an extension agent for experiments at water/air interfaces. We used NaOH (97%, Acros) and HCl (37%, Sigma Aldrich) to vary the pH of nanoparticle dispersions. We used all chemicals as received without further purification.

We used glass substrates with two distinct dimensions: 26×76×1 mm^3-microscope slides (Normax, Portugal) and 11×11×0.8 cm^3 win-

dows (Alucristal, Spain). The latter are made of extra-clear glass and we performed an extra-polishing on the edges using a Grinder-Polisher (Buehler AutoMet 250) following a protocol with different grit sizes. First, we used two grit sizes of silicon carbide papers (400 [P800] and 600 [P1200]). Subsequently, we employed a polishing cloth wetted with a diamond suspension (size 9 μm) to further improve the surface finish. After the polishing process, we cleaned the substrates using Milli-Q water, isopropyl alcohol and dried with N_2. We used these substrates for the deposition of microgel monolayers.

2.2. Nanoparticle characterization in dispersion

We determined the size and electrical properties of the microgels in dispersion by dynamic light scattering and laser doppler microelectrophoresis using a ZetaSizer Nano Z (Malvern Instruments). This technique provides detailed information about the hydrodynamic diameter d_H of the particles and their electrophoretic mobility μ_e, indicative of their surface charge and stability in dispersion. We used an autotitrator coupled to the ZetaSizer to automatically vary the pH of the nanoparticle dispersions. By incrementally adding precise amounts of hydrochloric acid (HCl, 0.1M) or sodium hydroxide (NaOH, 0.1M), we were able to systematically study the influence of pH on the microgel and TiO_2 nanoparticle properties. We conducted all measurements at a controlled temperature, ensuring that any observed changes in d_H and μ_e were attributable to the pH adjustments rather than to the thermoresponsiveness of the microgels. For each characterization, we prepared microgel and TiO_2 nanoparticle dispersions with a concentration of 0.1 wt% 15 minutes prior to each measurement.

2.3. Langmuir-Blodgett deposition and scaling-up for windows

We used a Langmuir-Blodgett trough (KSV NIMA, Biolin Scientific) for the self-assembly of microgels at a water/air interface and their subsequent deposition on glass substrates, i.e. the soft colloidal lithography (SCL) technique. First, we attached a glass substrate to the motorized dipper arm of the Langmuir-Blodgett trough and lowered it below the interface level at an angle of 60° respect to the interface. Next, we filled the trough with Milli-Q water fully covering the glass substrate. We measured the surface pressure (Π) with a Wilhelmy plate made of paper. We cleaned the interface by compressing the interface-area and aspirating the surface with a vacuum pump. Once we considered the interface clean enough, indicated by compressing the interface and obtaining $\Pi \leq 0.4$ mN m^{-1}, we deposited the microgel dispersion at the interface using a 100 μL glass microsyringe. We then added microgel dispersion up to $\Pi \simeq 5$ mN m^{-1}, letting it to rest for 10 min. Next, we transferred the microgel monolayer to a glass substrate by raising the substrate across the water/air interface at a rate of 0.5 mm/min. During the deposition, we kept Π constant thanks to the motorized barriers.

In addition, we characterized the compression curve of our microgels to obtain all possible ranges of separation between microgels while maintaining uniformity of the deposited monolayer. During these experiments, the monolayer was compressed while lifting the substrate across the interface. Immediately before the substrate fully crossed the interface, we fully opened the barriers to induce a rapid change in Π. This sudden change is a reference point enabling the correlation of each position on the substrate with its corresponding Π value (see Fig. S 1 in SI).

Next, we describe the novel negative templating assisted by SCL. We used the microgel monolayers deposited on glass substrates as negative templates for the final nanostructure composed of TiO_2 inorganic nanoparticles. This was achieved by immersing the microgel-laden glass substrate in a water dispersion of TiO_2 nanoparticles at 0.01 wt%. The TiO_2 nanoparticles attach to the substrate in the interstices of the microgels thanks to electrostatic interactions. To illustrate this, we measured the μ_e of the TiO_2 nanoparticles and microgels (see Fig. S 2 in SI). The inorganic nanoparticles have opposite charge than the substrates, while it is similar charge than the microgels. The steric repulsion of the microgels also plays a role in avoiding the deposition of TiO_2 nanoparticles on the microgels [50]. After 30 min, we rinsed the substrates with Milli-Q water and incinerated the microgels via air plasma ashing (Emitech K1050X) at 50 W for 15 min. After the plasma ashing, we obtained a nanohole-hexagonal array on the TiO_2 nanoparticle coating.

In order to scale up the SCL methodology for 11×11×0.8 cm^3 windows, we combined a bigger trough, a motorized dipping arm to control the deposition speed, and a custom made holder attached to the dipper. We used a light source and a silicon substrate as mirror on the bottom of the trough to reflect the light dispersed as rainbow colors by the microgel monolayer absorbed at the interface, guiding us in the proper formation of a microgel monolayer.

2.4. Luminescent layer deposition

The luminescent material was selected considering its optical properties and previously reported performance in LSC devices [51]. We deposited the DSLs based on Eu-doped styrene-ethylene-butylene-styrene (SEBS) polymer (synthesis details reported in [51] and in Supplementary Information) on the glass substrates using the doctor-blade deposition method. We deposited them on bare windows, on top of the TiO_2 coating, and on the opposite side of the window with TiO_2 coating.

Synthesis of Eu-based complex. We synthesized the Eu-based complex according to our previous method with some modifications [3]. We obtained a mixture of 3 mmol of TFNB and 1 mmol of Phen dissolved in 20 mL of ethanol (EtOH), then we added 3 mmol of NaOH aqueous solution under stirring. After that, we added 1 mmol of $EuCl_3$ aqueous solution. The solution was stirred at 50°C and we filtered the resulting precipitate, washing with EtOH and n-hexane, drying at 50°C to get the Eu-based complex, named as Eu-TFNB-Phen.

2.5. Atomic force microscopy (AFM) characterization

We characterized the substrates via an Atomic Force Microscope (AFM Dimension 3000) in tapping mode with home-made motorization [52]. The AFM was equipped with Tap300Al-G cantilevers (300 kHz, 40 Nm^{-1}, BudgetSensors, Bulgaria). We acquired images with a resolution of 512 x 512 $pixels^2$ over areas of 40 x 40 μm^2 and 10 x 10 μm^2. We post-processed the acquired images using Gwyddion to level them and enhance contrast.

2.6. Optical and electrical characterization

We recorded the photoluminescence spectra with a modular double-grating excitation spectrofluorimeter with a TRIAX 320 emission monochromator (Fluorolog-3, Horiba Scientific) coupled to a R928 Hamamatsu photomultiplier. We measured the absolute emission quantum yield (q) values at room temperature using a system (C9920-02, Hamamatsu) with a 150 W xenon lamp coupled to a monochromator for wavelength discrimination, an integrating sphere as the sample chamber, and a multichannel analyzer for signal detection. The method is accurate to within 10%. We characterized the diffuse and total reflectance in the UV-visible-NIR spectral range using a spectrophotometer (Lambda 950, Perkin-Elmer) equipped with an integrating sphere. Additionally, we used an ellipsometer (Horiba Jobin Yvon) to determine the refractive index (n) of the TiO_2 coatings, using a Cauchy-absorbent model for the fitting. We used a silicon wafer with ⟨100⟩ orientation (p-type, Boron doped, 1-10 Ω cm from University Wafer Inc., USA) for these measurements.

We characterized the current-voltage (I-V) curves of solar cells coupled to the edges of substrates at room temperature under simulated AM1.5G radiation (OSRAM Ultra-Vitalux 300W, ~225 W/m^2). For this, we connected a SourceMeter 2400 (SMU Instruments, Keithley) to a computer to control the measurements via a home-made MATLAB script. We framed the 11x11 cm^2 glass windows with polyvinyl chloride (PVC),

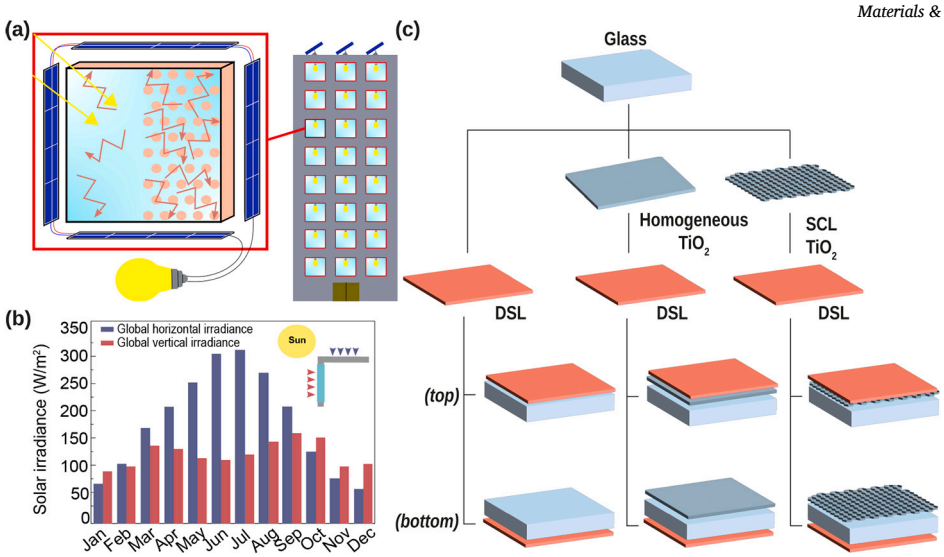

Fig. 1. (a) Schematic representation of the building integrated nanostructured TiO_2 thin layer plus DSLs coating on a window with PV cells on the sides of the window. The inorganic nanostructured coating is depicted on the right half of the window as hexagonal patterning. The red arrows indicate the total internal reflection (TIR) of both the captured and down-shifted sunlight, which it is increased by the nanostructured coating. **(b)** Global horizontal and vertical solar irradiance for a south-facing glazing unit over one year in Spain. Adapted with permission from [22]. **(c)** Schematic representation of sample preparation methodology and nomenclature.

attaching an array of 16 c-Si solar cells connected in series (IXOLARTM SolarBITs, ANYSOLAR, KXOB25-01X8F).

In order to study the behavior of light incidence on the edges of the coated substrates at different angles, we used a tilting platform with fixed angles at 0°, 15°, 30°, 45°, and 60°. We characterized the I-V curves as above explained for each substrate at all fixed angles. We fabricated two independent samples for each configuration and performed each experimental characterization in both of them, obtaining an average and standard deviation for each configuration to ensure consistency and reproducibility.

2.7. Optical modelling

The finite-differences time-domain method (FDTD) is a well-known and widely used method to understand the optical behavior of nano/microstructures [53,54]. It determines light propagation by numerically solving Maxwell's equations in the time domain. In this work, an FDTD solver [55] was employed to determine the reflection profile (specular and diffuse) of the fabricated samples. Since the FDTD method only determines the total reflection, it was necessary to develop a post-analysis process to calculate the fractions of specular and diffuse components of the outgoing light. This analysis uses both the simulation-determined electric and magnetic fields to determine the Poynting vector ($\vec{P}$ in Equation (1)).

$$\vec{P} = \frac{1}{2}\vec{E} \times \vec{H}^* \tag{1}$$

Here, $\vec{E}$ and $\vec{H}^*$ are the electric field vector and the complex conjugate of the magnetic field vector. The Poynting vector indicates the direction of power flow and is thus the ideal quantity to distinguish between the specular and diffuse components of light propagation. Furthermore, it can also be directly used to calculate the specific reflection ($R(f)$) of each of those components (Equation (2))

$$R(f) = \frac{P(f)_{\text{monitor}}}{P(f)_{\text{source}}} = \frac{\sum_x^N \sum_y^N P_z(f)\Delta_x\Delta_y}{P(f)_{\text{source}}} \tag{2}$$

where $P(f)_{\text{monitor}}$ is the power flow in a specific monitor (transmission or reflection), $P(f)_{\text{source}}$ is the source power (necessary to normalize the results), P_z is the z-component of the Poynting vector, since the monitor is the xy plane only the z-component of light is relevant for light propagation, Δ_x and Δ_y are the size of each grid element in the monitor.

The angle of light propagation (θ, Equation (3)) was also determined as it allows to better define a limit to separate specular and diffuse light. In this work, such separation value was set at 5°.

$$\theta = \arccos\left(\frac{P_z}{|\vec{P}|}\right) \tag{3}$$

The simulations were performed under periodic boundary conditions, anti-symmetric in x and symmetric in y, and perfect matching layer (PML) in z, considering 64 stretched coordinate PML layers, to better attenuate light scattered to bigger angles from the structures. We also performed an infinite medium approximation for the DSL and Glass layers, due to their significant thickness. Notably, higher thicknesses in low absorbing materials create several interference peaks in the reflection and transmission profiles, but the average behavior of the profiles remains similar [56,57].

3. Results and discussion

We show a schematic representation of LSC windows for BIPV application on vertical façades, being composed of a luminescent down-shifting layer (DSL) material as sketched in Fig. 1**a**, where the PV cells are attached to the window edges. The nanostructured inorganic coating is depicted by the hexagonal patterning on the right half of the window surface, which we use to increase the captured light as depicted by the number of arrows representing captured light. There are two main advantages: a larger area available for PV energy harvesting, and using a bigger portion of the irradiance that reaches the façades throughout the year, as depicted in Fig. 1**b**[22]. It is worth noting that the irradiance reaching the vertical façades can even overcome the horizontal irradiance on roofs during a significant portion of the year. Given all the configurations studied in this work, where we explore the role of having a nanostructured TiO_2 thin coating ($nTiO_2$) compared to a homogeneous one ($hTiO_2$), and having an additional DSL layer on top (tDSL) or bottom side (bDSL), we offer a scheme with the nomenclature that we use in Fig. 1**c**.

The DSL coating results in the down-shifting of UV light towards the visible and at the same time in the light-guiding towards the sides as shown in Fig. 2**a** on a 11x11 cm^2 glass window. We show the room temperature emission spectra of the DSL excited at the wavelength that

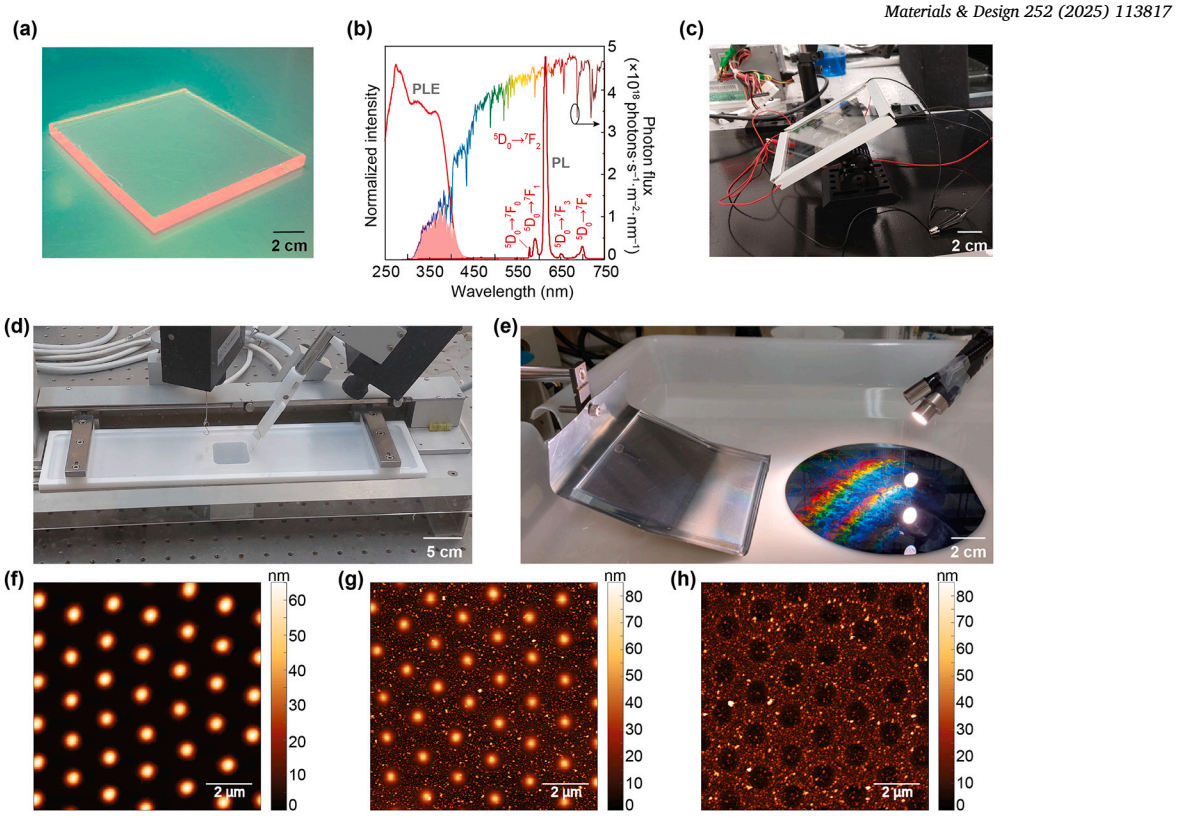

Fig. 2. (a) Window after DSL coating exposed to simulated solar radiation. Note the reddish down-shifted light redirected towards the sides of the window under perpendicular irradiation. **(b)** Excitation (PLE) and emission (PL) spectra of the DSL monitored at 612 nm and excited at 370 nm, respectively. The right y-axis represents the AM1.5G photon flux and the shadowed area is the overlap integral with PLE. **(c)** Electrical characterization set-up with PV cells mounted on the sides of the window, mounted on a tilting platform respect to a fixed vertical irradiation. **(d)** Soft Colloidal Lithography (SCL) on a Langmuir-Blodgett trough, limited to glass slides, and **(e)** a bigger trough to scale up the SCL to 11x11 cm^2 glass windows. We used a silicon wafer at the bottom as a mirror to reflect light and show the diffraction pattern produced by the self-assembled microgel monolayer. **(f)-(h)** AFM images of the SCL negative templating: **(f)** the microgel monolayer deposited on glass at $\Pi = 5\,mN/m$, **(g)** after immersion in the dispersion containing TiO_2 nanoparticles, and **(h)** after removing the microgels by plasma ashing.

maximizes the emission intensity in Fig. 2**b**, showing the expected Eu^{3+} $^5D_0 \rightarrow {}^7F_{0-4}$ transitions. Similarly to what was already reported [51], we did not observe any sign of the SEBS intrinsic emission regardless of the selected excitation wavelength (275 − 380 nm), suggesting an efficient SEBS-to-ligand/Ln^{3+} energy transfer. The absolute emission quantum yield values were also comparable to those already reported, $q = 0.54 \pm 0.05$. The absorption ability was evidenced in the excitation spectra monitored around the more intense transitions, which resembles that of the literature [51], with two main components peaking at 330 and 390 nm ascribed to the $\pi - \pi^*$ electronic transition of the Phen ligand [58], showing overlap with the AM1.5G solar irradiation with an overlap integral of ≈ 1.5% of the solar photon flux on Earth ($4.3 \cdot 10^{21}$ photons $s^{-1}\ m^{-2}$). A crucial test for our device is the characterization of the efficiency of the coatings in capturing, down-shifting and redirecting the light towards the sides of the windows. We coupled PV cells on the sides of the windows and mounted the window on a tilting platform that enabled us to study their energy harvesting efficiency as a function of the angle of incidence of the incoming light (see Fig. 2**c**).

In order to obtain nanostructured coatings on the windows we propose to use the SCL to assist in a novel negative templating methodology. Usually we perform the SCL on a Langmuir-Blodgett trough (see Fig. 2**d**) to set and keep a given surface pressure Π and to deposit the self-assembled monolayer by raising the substrate through the interface. Thus, the center-to-center distance of the microgels can be tuned by setting Π at the interface during the microgel deposition. As Π increases, the distance between microgels decreases (see Fig. S 1 in SI). Despite being the gold standard, this technique is constrained to the size of a glass slide. For this reason, for the first time we report an alternative process to scale up the SCL technique to 11x11 cm^2 glass windows (see Fig. 2**e**, and more details in Materials and Methods). We show a monolayer deposited at $\Pi = 5\,mN/m$ in Fig. 2**f** via AFM, with homogeneous feature size and interparticle distance. The microgels form a close-packed hexagonal array with a high degree of long-range order arising from the interplay between the capillary attraction and steric repulsion between the microgels adsorbed at water/air interfaces. Next, in order to use the microgel-laden substrates as negative templates, we immersed them in a dispersion containing the TiO_2 nanoparticles resulting in the coating of the interstices as shown in Fig. 2**g** thanks to electrostatic interactions. Finally, we removed the microgels by plasma ashing, leaving holes behind (see Fig. 2**h**). The thickness of the TiO_2 nanoparticle layer is ~ 80 nm, compatible with a single monolayer of TiO_2 nanoparticles. We label these substrates as $nTiO_2$, compared to homogeneous TiO_2 coating, labeled as $hTiO_2$. While for the sake of simplicity we will stick to hexagonal patterns in the main text, we demonstrate that the SCL negative templating can be expanded to more complex tessellations used as negative templates to create non-hexagonal nanostructures via sequential depositions of microgel monolayers [47] (see Fig. S 3 in SI). This novel technique facilitates the fabrication of large-area, low-cost inorganic nanoparticle coatings. Finally, since we want to elucidate the role of the combination of $nTiO_2$ or $hTiO_2$ thin layers with efficient DSL coatings [1], we deposited the DSL coatings on both bare windows, and on $nTiO_2$ and $hTiO_2$ coated windows as depicted in Fig. 1**c**.

Now we focus on the optical characterization of the different samples in the range between 250 and 2000 nm, including the NIR region which corresponds to light that contributes to heating the PV panels decreasing their efficiency. First, we present the total and diffuse reflectance from the FDTD simulations in Fig. 3**a** to assess what should be expected in the experimental characterization. In these simulations

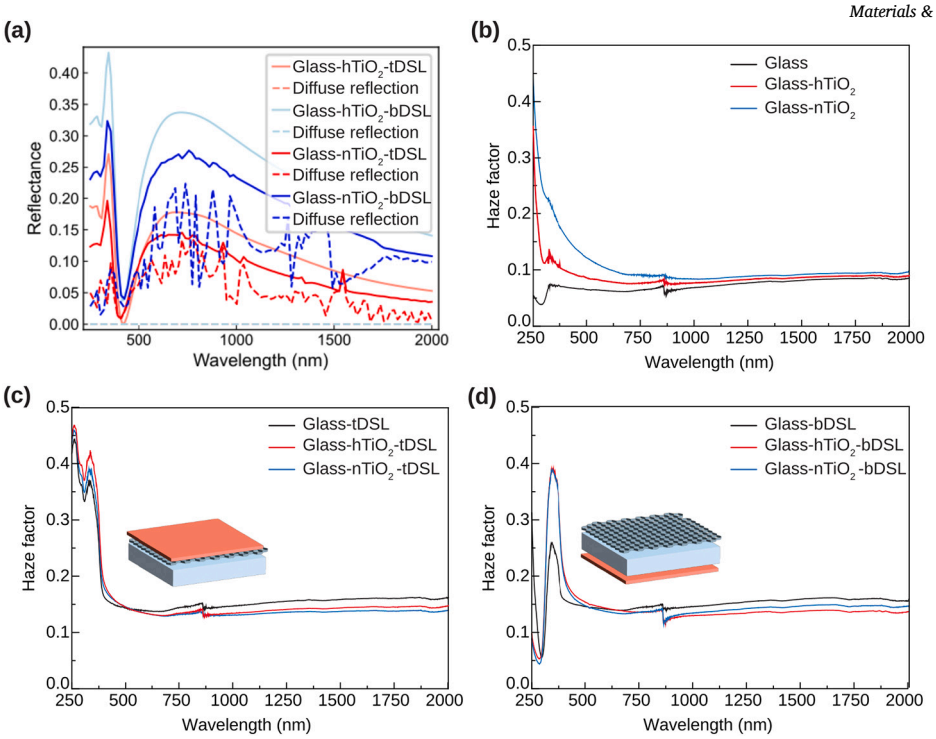

Fig. 3. (a) Total and Diffuse reflectance results from FDTD simulations. Haze factor of the **(b)** glass substrates with TiO_2, **(c)** glass substrates with TiO_2 and DSL on the top (tDSL) and **(d)** glass substrates with TiO_2 and DSL on the bottom (bDSL).

either the glass substrates or the top or bottom DSL layers are semi-infinite, while the nanostructured or homogeneous TiO_2 coatings are 80 nm-thick. We compared this semi-infinite approach to finite thickness for the materials (see Fig. S 4a-b in SI). The overall behavior under the semi-infinite approximation seems to better fit the experiments. The Glass-$hTiO_2$-bDSL configuration in finite media shows a reflection average similar to the semi-infinite simulation. The Glass-$hTiO_2$-tDSL exhibit higher values for the finite media compared to the semi-infinite approximation, since the top reflection from the DSL layer is not considered. This shows that it is possible to avoid the added complexity in the profiles and also avoid the exponentially higher simulation times required to analyze those structures, while keeping the overall correct trends. From now on we restrict to semi-infinite media simulations in Fig. 3**a**. These simulations show that the samples with $hTiO_2$ coatings always present higher reflection than their $nTiO_2$ counterparts, with their diffuse reflection being zero. Nanostructuring the TiO_2 layer effectively reduces the total reflectance of the surface, although this does not significantly impact on the transmittance of the samples, which is mainly influenced by the existence or not of the DSL. The dip in reflection at about 400 nm wavelengths can be ascribed to constructive interference arising from the TiO_2 layer thickness used, which provides the most significant change in refractive index from all the materials in the stack. This constructive interference results in much reduced reflection, as is customary observed with anti-reflection coatings. Moreover, by determining the scattering angle of light after passing through the structures, and assuming that higher average angles imply better scattering, it is possible to determine the ideal structural configuration for the size of the holes in the TiO_2 layer and its thickness (see Fig. S 5c-d in SI). As a general trend, we find that bigger holes and TiO_2 thickness should lead to more scattering. Furthermore, the highest diffuse reflectance is obtained for the Glass-$nTiO_2$-bDSL, since the higher refractive index of TiO_2, here taken to be $n \simeq 2.5$, leads to more refraction and increased anti-reflection, when compared to the one of glass and DSL, $n \simeq 1.5$, although the higher reflection of that sample should also have a small negative impact on the energy harvesting.

In order to start characterizing the fabricated samples, we measured experimentally the refractive index n (see Fig. S 5 in SI), where a similar increase in n is visible for the $nTiO_2$ and $hTiO_2$ coatings, compared to that of the bare glass window. It is worth noting that this refractive index is lower than the one of bare TiO_2 ($\simeq 2.5$) considered in the FDTD model. The lower experimental refractive index of our layer points out to an expected lower total and diffuse reflectance compared to the simulations, as it provides a reduced index contrast relative to the glass substrate. Experimentally, we quantify the surface reflection of the PV cells by the haze factor. The haze factor refers to the degree of incident light scattered forward towards the absorber layer. It can be described by the ratio between the diffuse reflectance ($R_{diffuse}$) and total reflectance (R_{total}): $Haze = R_{diffuse}/R_{total}$. Larger haze values correspond to increased scattering and hence an increased optical path length, which is of critical importance to improve the light absorption [59–61]. First, we considered glass windows with either $hTiO_2$ or $nTiO_2$ thin coatings in Fig. 3**b**. The haze factor increases from the bare glass when a homogeneous $hTiO_2$ coating is applied, and further increases for the nanostructured $nTiO_2$ coating, especially in the visible range. An increase in this factor indicates that the TiO_2 coating will scatter more light, thereby enhancing the light absorption of the solar cells. Fig. 3**c** and 3**d** show the haze factor of the glass substrates with TiO_2 and DSL on the top and at the bottom, respectively, showing that the main differences are on the DSL absorption spectral range, where the DSL induces an increase in the diffuse reflectance (see SI Fig. S 6 for extended data of transmittance, S 7 for total reflectance, S 8 for diffuse reflectance, S 9 for haze factor, and S 10 for visual appearance, respectively).

We electrically characterized all samples by their I-V curves for edge-coupled PV cells as a function of the angle of light incidence in Fig. 4, showing that the addition of both the TiO_2 coatings and the DSL induces an enhancement in the generated electrical power (P_{out}), as shown in Fig. 5**a** and Table S 1 in the Supporting Information. While the reduction in P_{out} at higher incidence angles is expected from pure geometrical considerations, future work is needed to assess the complex relation between optical and electrical parameters as a function of the angle of

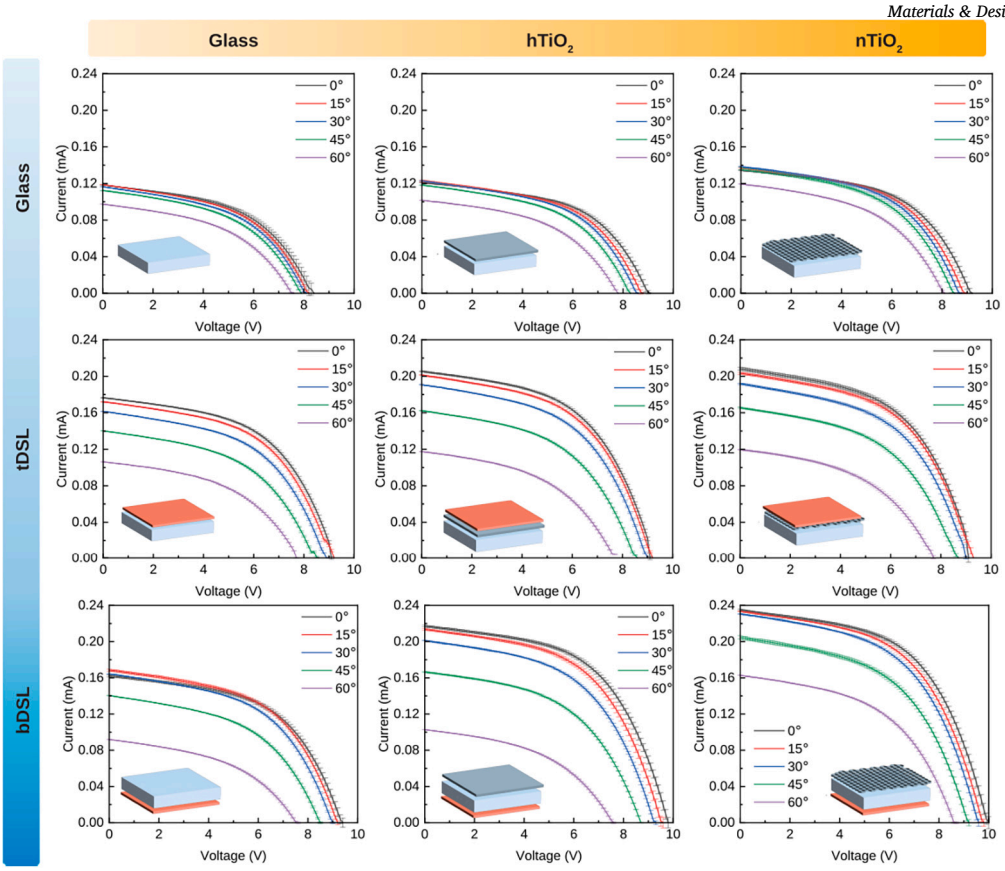

Fig. 4. I-V curves of the prepared samples under AM1.5G radiation as a function of the window tilting. The figure should be read as a matrix of combined horizontal and vertical elements.

incidence. We inferred the relative increase of P_{out} resulting of the application of the TiO_2 and/or luminescent DSL as follows:

$$\Delta P\,(\%) = \frac{P_{coated} - P_{bare}}{P_{bare}} \times 100$$

in which P_{coated} is the power generated by the LSC device with the TiO_2 or DSL coating, and P_{bare} is the power generated by the corresponding device without the referred coating.

The substrates coated solely with TiO_2 coatings exhibit an increase of ΔP up to 17% and 33%, for the $hTiO_2$ and $nTiO_2$ coatings, respectively, compared to the bare glass window (Fig. 5 and Table S 1 in Supporting Information).

We observed a significant enhancement in P_{out} for the substrates with DSL in comparison to the bare glass (Fig. 5 and Table S 1 in Supporting Information). In the absence of the TiO_2 coatings, the tested configurations of adding the DSL on top or at the bottom of the glass did not reveal any significant differences in P_{out}, except for the case at 60° tilting. Also, with the tDSL, there is no significant differences in P_{out} when using $hTiO_2$ or $nTiO_2$ (Fig. 5 and Table S 1 in Supporting Information). This might be due to the fact that the DSL layer is chosen to match *n* of the bare glass, and thus it fills the voids and match *n* in this configuration, defeating the diffraction produced by the TiO_2 coating. However, the efficiency of the bDSL significant changed depending on having the $nTiO_2$ compared to the $hTiO_2$ coating, achieving the highest performance of all substrates and configurations tested. In general, the results indicate that, independently of the angle of incident light, the $nTiO_2$ coating consistently enhances the P_{out} of the solar cells attached to the edges of the glass substrate. We find increased ΔP values around 57% (with a power conversion efficiency PCE of 0.07%) for angles in the 0° to 45° range, and above 100% for the case at 60° tilting (0.038% PCE), compared to the glass with only the bDSL (with 0.044% and 0.017% PCE at 0° and 60º, respectively). See Fig. 5 and Table S 1 in Supporting Information for an extensive data comparison. Overall, from the experimental results, we can conclude that the enhanced diffusivity provided by the $nTiO_2$ coating on a bDSL configuration is more beneficial than the reflection losses predicted in the simulations.

4. Conclusions

In this work we address efficiency issues of DSL-based BIPV solutions by tackling the problem of down-shifted light lost through the escape cone in the lightguide. We propose to use nanostructured inorganic TiO_2 nanoparticle coatings in combination with the DSL-coated windows to increase their efficiency in capturing and redirecting the down-shifted light towards PV panels installed on the sides of the window, transforming them into energy-generating units while maintaining their transparency and functionality. Since it is crucial to have a low-cost and scalable methodology for this endeavor, we successfully developed the soft colloidal lithography negative templating technique to produce nanostructured inorganic TiO_2 nanoparticle coatings. We achieved a significant milestone by scaling the technique to 11x11 cm^2 glass windows to explore their use in BIPV. This breakthrough promises to enhance the efficiency and aesthetic integration of solar energy solutions in modern building designs, contributing to more sustainable and energy-efficient urban environments. We explored a large combination of configurations regarding the TiO_2 and DSL coatings both in simulations and experiments, and obtained the highest enhancement of power output when we used nanostructured TiO_2 coatings on the window in combination with a DSL on the bottom side. Our experiments demonstrate the capability of capturing and down-shifting simulated sunlight from a broad range of incident angles. In particular we found increases in P_{out} of around 57% for angles of incidence below 45°, and above 100% for 60°, compared to the window with only the DSL layer on the bottom side.

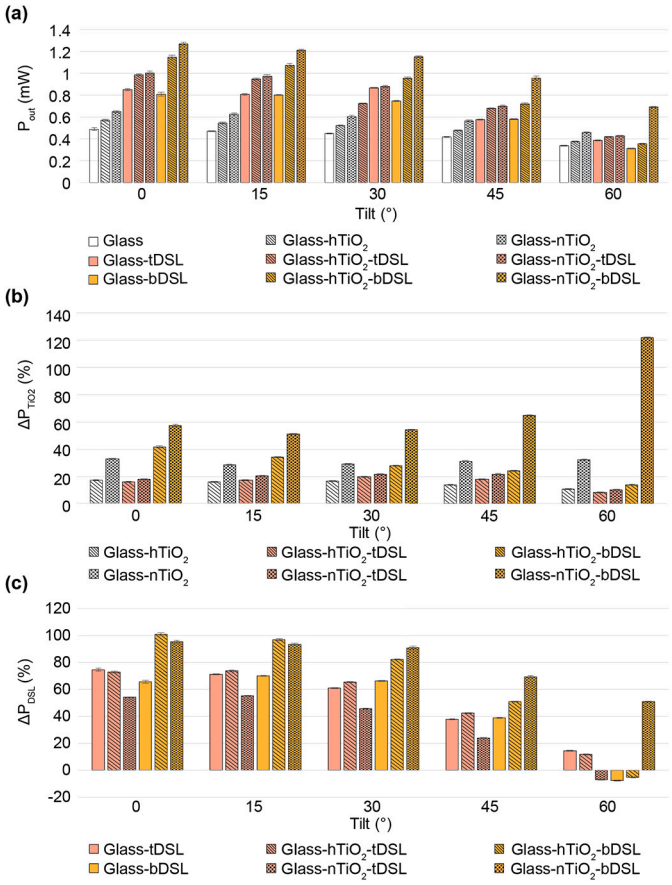

Fig. 5. (a) P_{out}, **(b)** ΔP_{TiO_2} and **(c)** ΔP_{DSL} of the LSCs edge-coupled PV cells for each prepared samples according to the tilting angle.

This capability ensures that even when sunlight strikes the window at glancing angles, a significant portion of the light is still absorbed and re-emitted towards the PV cells. This approach ensures that BIPV windows not only contribute to the aesthetic appeal and functionality of modern buildings but also provide a robust and efficient solution for harvesting the solar energy throughout the day/year, regardless of the sun's position.

CRediT authorship contribution statement

J.G. Guerrero-Felix: Writing – review & editing, Writing – original draft, Visualization, Investigation, Data curation. **S.F.H. Correia:** Writing – review & editing, Writing – original draft, Visualization, Validation, Investigation, Formal analysis, Data curation. **M. Alexandre:** Writing – review & editing, Writing – original draft, Visualization, Software, Investigation, Data curation. **C.D. Gonzalez-Gomez:** Writing – original draft, Visualization, Software, Investigation. **V. Sencadas:** Resources. **L. Fu:** Resources. **E. Ruiz-Reina:** Resources. **P.S. André:** Resources. **C.L. Moraila-Martinez:** Writing – review & editing, Supervision, Project administration, Funding acquisition, Data curation. **M.J. Mendes:** Writing – review & editing, Writing – original draft, Visualization, Validation, Supervision, Software, Resources, Data curation, Conceptualization. **R.A.S. Ferreira:** Writing – review & editing, Writing – original draft, Visualization, Validation, Supervision, Resources, Project administration, Methodology, Funding acquisition, Formal analysis, Data curation, Conceptualization. **M.A. Fernandez-Rodriguez:** Writing – review & editing, Writing – original draft, Visualization, Validation, Supervision, Resources, Project administration, Methodology, Funding acquisition, Formal analysis, Data curation, Conceptualization.

Declaration of competing interest

The authors declare that they have no known competing financial interests or personal relationships that could have appeared to influence the work reported in this paper.

Acknowledgements

This work was supported by the projects PID2020-116615RA-I00 funded by MICIU/AEI/10.13039/501100011033, EMERGIA grant with reference EMC21_00008 and project C-ING-208-UGR23 funded by Consejería de Universidad, Investigación e Innovación de la Junta de Andalucía, co-financed by FEDER "Andalucía 2021-2027". Also by grants PID2023-149387OB-I00 and PID2023-147135OB-I00 funded by MICIU/AEI/10.13039/501100011033 and by FEDER, EU. Also by a Short Term Scientific Mission from the COST Action CA18223 SyMat (European Cooperation in Science and Technology), funded by the Horizon 2020 Framework Programme of the European Union. We also acknowledge funding by FCT (Fundação para a Ciência e Tecnologia, I.P.) under the projects LA/P/0037/2020, UIDP/50025/2020 and UIDB/50025/2020 of the Associate Laboratory Institute of Nanostructures, Nanomodelling and Nanofabrication—i3N, and by the projects SpaceFlex (2022.01610.PTDC) and M-ECO2 – Industrial cluster for advanced biofuel production, Ref. C644930471-00000041, co-financed by PRR – Recovery and Resilience Plan of the European Union (Next Generation EU). This work was also developed within the scope of the projects CICECO – Aveiro Institute of Materials, UIDB/50011/2020 (DOI: 10.54499/UIDB/50011/2020), UIDP/50011/2020 (DOI: 10.54499/UIDP/50011/2020) and LA/P/0006/2020 (DOI: 10.54499/LA/P/0006/2020) and Instituto de Telecomunicações, UIDB/50008/2020 (10.54499/UIDB/50008/2020), UIDP/50008/2020 (10.54499/UIDP/50008/2020) and LA/P/0109/2020 (DOI: 10.54499/LA/P/0109/2020), Applied Molecular Biosciences Unit – UCIBIO, UIDP/04378/2020 (DOI: 10.54499/UIDP/04378/2020) and UIDB/04378/2020 (DOI: 10.54499/UIDB/04378/2020), financed by national funds through the FCT/MEC (PIDDAC), and when appropriate co-financed by FEDER under the PT2020 Partnership through European Regional Development Fund (ERDF) in the frame of Operational Competitiveness and Internationalization Programme (POCI). S.F.H.C. thanks FCT (2022.03740.CEECIND).

Appendix A. Supplementary material

Supplementary material related to this article can be found online at https://doi.org/10.1016/j.matdes.2025.113817.

Data availability

Data will be made available on request.

References

[1] G. Figueiredo, S.F.H. Correia, L. Fu, V. de Zea Bermudez, A.N.C. Neto, P.S. André, R.A.S. Ferreira, Luminescent solar concentrators: current and future applications in smart cities, in: Handbook on the Physics and Chemistry of Rare Earths, Elsevier, 2024.

[2] Y.A. Marei, M. Emam, M.E. Ahmed, A.A. Attia, M. Abdelrahman, Thermal and optical investigations of various transparent wall configurations and building integrated photovoltaic for energy savings in buildings, Energy Convers. Manag. 299 (2024) 117817.

[3] R.A.S Ferreira, S.F.H. Correia, A. Monguzzi, X. Liu, F. Meinardi, Spectral converters for photovoltaics–what's ahead, Mater. Today 33 (2020) 105–121.

[4] F. Meinardi, F. Bruni, S. Brovelli, Luminescent solar concentrators for building-integrated photovoltaics, Nat. Rev. Mater. 2 (12) (2017) 1–9.

[5] Y. Li, X. Huang, H.K. Sheriff Jr, S.R. Forrest, Semitransparent organic photovoltaics for building-integrated photovoltaic applications, Nat. Rev. Mater. 8 (3) (2023) 186–201.

[6] H.M. Maghrabie, K. Elsaid, E.T. Sayed, M.A. Abdelkareem, T. Wilberforce, A. Olabi, Building-integrated photovoltaic/thermal (bipvt) systems: applications and challenges, Sust. Energy Technol. Assess. 45 (2021) 101151.

[7] M. Tripathy, P. Sadhu, S. Panda, A critical review on building integrated photovoltaic products and their applications, Renew. Sustain. Energy Rev. 61 (2016) 451–465.
[8] E. Almeida, M. Alexandre, I.M. Santos, R. Martins, H. Águas, M.J. Mendes, Photonic-enhanced perovskite solar cells: tailoring color and light capture, ACS Omega 9 (42) (2024) 42839–42849.
[9] D. Singh, R. Chaudhary, A. Karthick, Review on the progress of building-applied/integrated photovoltaic system, Environ. Sci. Pollut. Res. Int. 28 (2021) 47689–47724.
[10] Z. Liu, Y. Zhang, X. Yuan, Y. Liu, J. Xu, S. Zhang, B.-j. He, A comprehensive study of feasibility and applicability of building integrated photovoltaic (bipv) systems in regions with high solar irradiance, J. Clean. Prod. 307 (2021) 127240.
[11] Y. Meng, Y. Tan, X. Li, Y. Cai, J. Peng, Y. Long, Building-integrated photovoltaic smart window with energy generation and conservation, Appl. Energy 324 (2022) 119676.
[12] X. Zhao, Y. Lai, K. Zheng, Q. Song, L. Wang, Y. Chen, H. Chen, R. Wang, Y. Zhou, Highly transparent, spectrally selective power-generating windows based on wo3–x nanorods and carbon dots for full-spectrum utilization, ACS Appl. Mater. Interfaces (2025).
[13] S. Haque, M. Alexandre, A.T. Vicente, K. Li, C.S. Schuster, S. Yang, H. Águas, R. Martins, R.A.S. Ferreira, M.J. Mendes, Photon shifting and trapping in perovskite solar cells for improved efficiency and stability, Light: Sci. Appl. 13 (1) (2024) 238.
[14] F. Meinardi, S. Ehrenberg, L. Dhamo, F. Carulli, M. Mauri, F. Bruni, R. Simonutti, U. Kortshagen, S. Brovelli, Highly efficient luminescent solar concentrators based on Earth-abundant indirect-bandgap silicon quantum dots, Nat. Photonics 11 (3) (2017) 177–185.
[15] J. Lin, L. Wang, Q. Jing, H. Zhao, Highly efficient and high color rendering index multilayer luminescent solar concentrators based on colloidal carbon quantum dots, Chem. Eng. J. 481 (2024) 148441.
[16] H. Zhao, G. Liu, S. You, F.V.A. Camargo, M. Zavelani-Rossi, X. Wang, C. Sun, B. Liu, Y. Zhang, G. Han, A. Vomiero, X. Gong, Gram-scale synthesis of carbon quantum dots with a large Stokes shift for the fabrication of eco-friendly and high-efficiency luminescent solar concentrators, Energy Environ. Sci. 14 (2021) 396–406.
[17] P. Bernardoni, G. Mangherini, M. Gjestila, A. Andreoli, D. Vincenzi, Performance optimization of luminescent solar concentrators under several shading conditions, Energies 14 (4) (2021) 816.
[18] E. Klampaftis, D. Ross, K.R. McIntosh, B.S. Richards, Enhancing the performance of solar cells via luminescent down-shifting of the incident spectrum: a review, Sol. Energy Mater. Sol. Cells 93 (8) (2009) 1182–1194.
[19] S.F.H. Correia, P.P. Lima, P.S. André, R.A.S. Ferreira, L.D. Carlos, High-efficiency luminescent solar concentrators for flexible waveguiding photovoltaics, Sol. Energy Mater. Sol. Cells 138 (2015) 51–57.
[20] J. Farinhas, S.F.H. Correia, L. Fu, A.M. Botas, P.S. André, R.A.S. Ferreira, A. Charas, Ultraviolet-filtering luminescent transparent coatings for high-performance ptb7-th: itic–based organic solar cells, Frontiers in Nanotechnology 3 (2021) 635929.
[21] X. Huang, S. Han, W. Huang, X. Liu, Enhancing solar cell efficiency: the search for luminescent materials as spectral converters, Chem. Soc. Rev. 42 (1) (2013) 173–201.
[22] M. Díez-Mediavilla, M. d, C. Rodríguez-Amigo, M. Dieste-Velasco, T. García-Calderón, C. Alonso-Tristán, The pv potential of vertical façades: a classic approach using experimental data from Burgos, Spain, Sol. Energy 177 (2019) 192–199.
[23] S.F.H. Correia, V. de Zea Bermudez, S.J. Ribeiro, P.S. André, R.A.S. Ferreira, L.D. Carlos, Luminescent solar concentrators: challenges for lanthanide-based organic–inorganic hybrid materials, J. Mater. Chem. A 2 (16) (2014) 5580–5596.
[24] M.G. Debije, P.P. Verbunt, B.C. Rowan, B.S. Richards, T.L. Hoeks, Measured surface loss from luminescent solar concentrator waveguides, Appl. Opt. 47 (36) (2008) 6763–6768.
[25] H.C. Bauser, C.R. Bukowsky, M. Phelan, W. Weigand, D.R. Needell, Z.C. Holman, H.A. Atwater, Photonic crystal waveguides for > 90% light trapping efficiency in luminescent solar concentrators, ACS Photonics 7 (8) (2020) 2122–2131.
[26] A. Peter Amalathas, M.M. Alkaisi, Nanostructures for light trapping in thin film solar cells, Micromachines 10 (9) (2019) 619.
[27] L. Zhu, J. Zhang, D. Wang, R. Wang, Y. Sun, C. Wu, Optimal design and photoelectric performance study of micro-lens light trapping structure for cigs thin film solar cell in bipv, Renew. Energy 177 (2021) 1356–1371.
[28] S.-W. Choi, J.-H. Park, J.-H. Kim, Y. Kim, P. Song, M. Shin, J.-D. Kwon, Evaluation method of the light-trapping structure for a transparent thin-film silicon solar cell with low-illuminance condition, Sol. Energy 231 (2022) 1107–1114.
[29] Y. Zhu, Q. Zhang, L. Shu, D. Zhang, Z. Fan, Recent progress of efficient flexible solar cells based on nanostructures, J. Semicond. 42 (10) (2021) 101604.
[30] M. Alexandre, M. Chapa, S. Haque, M.J. Mendes, H. Águas, E. Fortunato, R. Martins, Optimum luminescent down-shifting properties for high efficiency and stable perovskite solar cells, ACS Applied Energy Materials 2 (4) (2019) 2930–2938.
[31] F.A. Mutlak, A.F. Ahmed, U.M. Nayef, Q. Al-zaidi, S.K. Abdulridha, Improvement of absorption light of laser texturing on silicon surface for optoelectronic application, Optik 237 (2021) 166755.
[32] O. Sanchez-Sobrado, M.J. Mendes, S. Haque, T. Mateus, A. Araujo, H. Aguas, E. Fortunato, R. Martins, Colloidal-lithographed tio 2 photonic nanostructures for solar cell light trapping, J. Mater. Chem. C 5 (27) (2017) 6852–6861.
[33] D. Visser, D.Y. Chen, Y. Désières, A.P. Ravishankar, S. Anand, Embossed mie resonator arrays composed of compacted tio2 nanoparticles for broadband anti-reflection in solar cells, Sci. Rep. 10 (1) (2020) 1–11.
[34] G. Perrakis, A.C. Tasolamprou, G. Kenanakis, E.N. Economou, S. Tzortzakis, M. Kafesaki, Combined nano and micro structuring for enhanced radiative cooling and efficiency of photovoltaic cells, Sci. Rep. 11 (1) (2021) 11552.
[35] A. Alshammari, E. Almatrafi, M. Rady, Radiative coatings for solar cell cooling: materials, and applications, Sol. Energy 273 (2024) 112545.
[36] R. Mabindisa, K. Tambwe, L. Mciteka, N. Ross, Organic nanostructured materials for sustainable application in next generation solar cells, Appl. Sci. 11 (23) (2021) 11324.
[37] S. Liu, Y. Sun, L. Chen, Q. Zhang, X. Li, J. Shuai, A review on plasmonic nanostructures for efficiency enhancement of organic solar cells, Materials Today Physics 24 (2022) 100680.
[38] S.L. Mortazavifar, M.R. Salehi, M. Shahraki, E. Abiri, Optimization of light absorption in ultrathin elliptical silicon nanowire arrays for solar cell applications, J. Mod. Opt. 69 (7) (2022) 368–380.
[39] S. Behera, P.W. Fry, H. Francis, C.-Y. Jin, M. Hopkinson, Broadband, wide-angle antireflection in gaas through surface nano-structuring for solar cell applications, Sci. Rep. 10 (1) (2020) 6269.
[40] Y. Gu, J. Xu, J. Lin, H. Ma, H. Zhao, Y. Zhang, B. Sun, The fabrication of anti-reflection grating structures film for solar cells using vibration-assisted uv nanoimprint lithography, Sol. Energy 241 (2022) 172–183.
[41] R.D. Oliveira, A. Mouquinho, P. Centeno, M. Alexandre, S. Haque, R. Martins, E. Fortunato, H. Águas, M.J. Mendes, Colloidal lithography for photovoltaics: an attractive route for light management, Nanomaterials 11 (7) (2021).
[42] O. Pylypova, O. Havryliuk, S. Antonin, A. Evtukh, V. Skryshevsky, I. Ivanov, S. Shmahlii, Influence of nanostructure geometry on light trapping in solar cells, Appl. Nanosci. (2022) 1–6.
[43] H. Liu, Y. Du, X. Yin, M. Bai, W. Liu, et al., Micro/nanostructures for light trapping in monocrystalline silicon solar cells, J. Nanomater. (2022) 2022.
[44] J.L.N. Boane, P. Centeno, A. Mouquinho, M. Alexandre, T. Calmeiro, E. Fortunato, R. Martins, M.J. Mendes, H. Águas, Soft-microstructured transparent electrodes for photonic-enhanced flexible solar cells, Micro 1 (2) (2021) 215–227.
[45] Y. Wang, M. Zhang, Y. Lai, L. Chi, Advanced colloidal lithography: from patterning to applications, Nano Today 22 (2018) 36–61.
[46] J. Zhang, Y. Li, X. Zhang, B. Yang, Colloidal self-assembly meets nanofabrication: from two-dimensional colloidal crystals to nanostructure arrays, Adv. Mater. 22 (38) (2010) 4249–4269.
[47] F. Grillo, M.A. Fernandez-Rodriguez, M.-N. Antonopoulou, D. Gerber, L. Isa, Self-templating assembly of soft microparticles into complex tessellations, Nature 582 (7811) (2020) 219–224.
[48] M.Á. Fernández-Rodríguez, R. Elnathan, R. Ditcovski, F. Grillo, G.M. Conley, F. Timpu, A. Rauh, K. Geisel, T. Ellenbogen, R. Grange, et al., Tunable 2d binary colloidal alloys for soft nanotemplating, Nanoscale 10 (47) (2018) 22189–22195.
[49] A. Rubio-Andrés, D. Bastos-González, M.A. Fernandez-Rodriguez, Tuning the bulk behavior and 2d interfacial self-assembly of microgels by keggin-type polyoxometalate ionic specificity, J. Mol. Liq. 400 (2024) 124496.
[50] H. Horiuchi, A. Nikolov, D. Wasan, Calculation of the surface potential and surface charge density by measurement of the three-phase contact angle, J. Colloid Interface Sci. 385 (1) (2012) 218–224.
[51] G. Figueiredo, S.F.H. Correia, B.P. Falcão, V. Sencadas, L. Fu, P.S. André, R.A.S. Ferreira, Multi-surface adhesion luminescent solar concentrators for supply-less IoT, Adv. Sci. (2024) 2400540.
[52] J.G. Guerrero-Felix, J. Lopez-Miras, M.A. Rodriguez-Valverde, C.L. Moraila-Martinez, M.A. Fernandez-Rodriguez, Automation of an atomic force microscope via Arduino, HardwareX 15 (2023) e00447.
[53] S. Haque, M. Alexandre, M.J. Mendes, H. Águas, E. Fortunato, R. Martins, Design of wave-optical structured substrates for ultra-thin perovskite solar cells, Appl. Mater. Today 20 (2020) 100720.
[54] S. Haque, M. Alexandre, C. Baretzky, D. Rossi, F. De Rossi, A.T. Vicente, F. Brunetti, H. Águas, R.A.S. Ferreira, E. Fortunato, M. Auf der Maur, U. Würfel, R. Martins, M.J. Mendes, Photonic-structured perovskite solar cells: detailed optoelectronic analysis, ACS Photonics 9 (7) (2022) 2408–2421.
[55] Ansys Lumerical FDTD, https://www.ansys.com/products/optics/fdtd.
[56] M. Chapa, M.F. Alexandre, M.J. Mendes, H. Águas, E. Fortunato, R. Martins, All-thin-film perovskite/C–Si four-terminal tandems: interlayer and intermediate contacts optimization, ACS Applied Energy Materials 2 (6) (2019) 3979–3985.
[57] P. Centeno, M.F. Alexandre, M. Chapa, J.V. Pinto, J. Deuermeier, T. Mateus, E. Fortunato, R. Martins, H. Águas, M.J. Mendes, Self-cleaned photonic-enhanced solar cells with nanostructured parylene-C, Adv. Mater. Interfaces 7 (15) (2020) 2000264.
[58] J. Garcia-Torres, P. Bosch-Jimenez, E. Torralba-Calleja, M. Kennedy, H. Ahmed, J. Doran, D. Gutierrez-Tauste, L. Bautista, M. Della Pirriera, Modulating the photoluminescence of europium-based emitting polymers: influence of the matrix on the photophysical properties, J. Photochem. Photobiol. A, Chem. 275 (2014) 103–113.
[59] D.B. Mahadik, R. Lakshmi, H.C. Barshilia, High performance single layer nanoporous antireflection coatings on glass by sol–gel process for solar energy applications, Sol. Energy Mater. Sol. Cells 140 (2015) 61–68.
[60] C. Preston, Y. Xu, X. Han, J.N. Munday, L. Hu, Optical haze of transparent and conductive silver nanowire films, Nano Res. 6 (2013) 461–468.
[61] S.F.H. Correia, A.R. Bastos, L. Fu, L.D. Carlos, P.S. André, R.A.S. Ferreira, Lanthanide-based downshifting layers tested in a solar car race, Opto-Electronic Advances 2 (6) (2019) 190006.